Relative elastic interferometric imaging for microseismic source location

Lei Li[1,2], Hao Chen[1] and Xiuming Wang[1]

[1] State Key Laboratory of Acoustics, Institute of Acoustics, Chinese Academy of Sciences, Beijing 100190, People's Republic of China
[2] University of Chinese Academy of Sciences, Beijing 100049, People's Republic of China

E-mail: chh@mail.ioa.ac.cn

CrossMark

Abstract

Combining a relative location method and seismic interferometric imaging, a relative elastic interferometric imaging method for microseismic source location is proposed. In the method, the information of a known event (the main event) is fully used to improve the location precision of the unknown events (the target events). First, the principles of both conventional and the relative interferometric imaging methods are analyzed. Traveltime differences from the position of the same potential event to different receivers are used in direct interferometric imaging, while relative interferometric imaging utilizes those of different events to the same receiver. Second, 2D and 3D numerical experiments demonstrate the feasibility of this newly proposed method in locating a single microseismic event. Envelopes of cross-correlation traces are utilized to eliminate the effects of changing polarities resulting from the source mechanism and receiver configuration. Finally, the location precision of the relative and conventional interferometric imaging methods are compared, and it indicates that the former hold both advantages of the relative method and interferometric imaging. Namely, it can adapt to comparatively high velocity error and low signal-to-noise ratio (SNR) microseismic data. Moreover, since there is no arrival time picking and fewer cross-correlograms are imaged, the method also significantly saves computational expense.

Keywords: microseismic location, relative location, interferometric imaging, cross-correlation, traveltime difference

(Some figures may appear in colour only in the online journal)

1. Introduction

Microseismic monitoring has been widely used in many geophysical areas such as rock burst monitoring and warning in the mining industry and tunnels, geothermal exploration monitoring, microseismicity analysis of geological structure and oil and gas reservoir monitoring (Gibowicz *et al* 1994, Duncan and Eisner 2010, Maxwell *et al* 2010, Maxwell 2014, Feng *et al* 2015, Tian and Ritzwoller 2015). Hydraulic fracturing and horizontal well drilling are the two key technologies of exploration and development for unconventional oil and gas resources (Warpinski 2014), and microseismic monitoring is one of the most effective technologies to monitor the geometry of fractures, evaluate the stimulated reservoir volume (SRV) as well as optimize the field operations. Combined with

geomechanics and reservoir models, the locations of microseismic events can be applied to determine the geometry and distribution of fractures, help to model fracture propagation and simulate reservoir, design fracture network, and forecast and identify geological hazards (Le Calvez *et al* 2007, Cipolla *et al* 2010, 2012), etc. Therefore, the application of microseismic monitoring permeates the whole exploration, development and exploitation stages for unconventional oil and gas resources. Microseismic data processing mainly includes velocity model building, signal pre-processing, microseismic forward modeling and location, source mechanism inversion and velocity anisotropy analysis (Grechka *et al* 2011, Zhao and Young 2011, Li *et al* 2013, Chambers *et al* 2014, Song *et al* 2014). Microseismic source location is the basis and kernel in data processing.

As it has rapidly developed and progressed in recent years, the research focus of location methods has transferred from traveltime inversion to stacking-based or migration-based imaging methods (Kao and Shan 2004, 2007, Bardainne *et al* 2009, Artman *et al* 2010, Grigoli *et al* 2013, 2014, Zhang and Zhang 2013, Staněk *et al* 2015). Traveltime inversion only utilizes kinematic information (response to geological structure, such as traveltime) of microseismic wavefield, while imaging methods utilize both kinematic information and dynamic information (response to lithologic characteristics, such as amplitude). The migration-based method can also be called beamforming or coherence scanning. These methods can image and locate the sources by focusing the energy into discrete grids with spatial filtering. Compared with classical traveltime inversion, imaging methods have three main advantages: (1) These methods are data-driven and more objective, since they do not need to do traveltime or phase picking and can avoid errors from it; (2) due to the stacking process in imaging, they can adapt to low-SNR microseismic data, especially for surface monitoring with a large receiver aperture and number; (3) it is convenient to unite the imaging methods with source mechanism inversion and other reservoir characterization methods (such as reflection seismic imaging) (Duncan and Eisner 2010).

Seismic interferometry has become a new research hotspot in exploration geophysics in recent years, which is an extension and application of interferometry in seismic data processing. Its core idea or principle is extracting hidden information in noise, refraction records or seismic coda to reconstruct applicable seismograms for subsequent processing and interpretation (Claerbout 1968, Schuster 2001, Campillo and Paul 2003, Wapenaar *et al* 2010a, 2010b). The proposal of seismic interferometry not only enriches the theory and applications of both seismic exploration and global seismology, but exhibits great potential in passive seismic imaging. Grechka and Zhao (2012) utilized interferometry to synthesize vertical seismic profiling (VSP) records from downhole microseismic data, and expected good application prospects of interferometry in microseismic monitoring. According to the features of records generated through interferometry (called correlogram or interferogram), subsurface reflectors or sources can be imaged by applying the corresponding migration kernels (Schuster *et al* 2004, Borcea *et al* 2006, Chang *et al* 2009). This method is referred to as interferometric imaging or cross-correlation migration. Schuster and Zhou (2006) also verified that these methods possessed identical essence, which is the cross-correlation and summation over all sources and/or receivers. The differences between these methods lay in the choice of weights when cross-correlating the traces. Moreover, correlation-based methods do not require theoretical traveltime for migration and avoid static correction, since they can directly image based on time shifts that come from correlation of the data. Grandi and Oates (2009) and Xiao *et al* (2009) preliminarily verified the feasibility of interferometric imaging in surface microseismic monitoring.

At present, most microseismic location methods locate events individually and independently. Actually, the relative location method has already been used in locating natural and mining earthquakes since the 1970s (Fitch 1975, Spence 1980, Gibowicz *et al* 1994). The traveltime difference between a known earthquake (called a main event) and an unknown earthquake (called a target event) to the same receiver is used, and the location uncertainty can be alleviated because of the additional information from the known sources. Representative relative location methods developed latterly include the double-difference method (Waldhauser and Ellsworth 2000, Zhang and Thurber 2003) and interferometry microseismic location (Poliannikov *et al* 2011, 2013). The former located a source by minimizing the residual sum of the traveltime difference from potential source positions to all receivers. The latter utilized interferometry, but it was different from interferometric imaging. The stationary receiver, which contained the stationary time lag, was found in the cross-correlogram of the main event and target event. Then, the traveltime difference and position of the main event were used to locate the target event. In field application, many reference microseismic events can be obtained since multiple fractures are created, so the idea of relative location may have great potential in microseismic location.

In this study, relative location and elastic interferometric imaging are united through bringing in a known main event. Then, a relative elastic interferometric imaging method (REII) for microseismic location is proposed. First, the principles of conventional and relative interferometric imaging methods are introduced, and the relations and differences between them are analyzed. A 2D model is used to verify the feasibility of REII in locating a single event. In order to the eliminate effects of changing polarities resulting from the source mechanism and receiver configuration, the original values of cross-correlation traces are replaced by their envelopes in the imaging process. Then, a 3D model with an event of dip-slip source mechanism is simulated. The imaging results of single-well, double-well and surface monitoring arrays are compared and analyzed. At last, the dependency on the velocity model and computational expenses of relative and conventional interferometric imaging methods are compared in a 3D numerical experiment.

2. Basic principles

Seismic interferometric imaging differs from traditional migration in migration kernel functions since it migrates and images the cross-correlograms instead of the original seismograms. The basic principles and procedures for seismic source location of conventional elastic interferometric imaging are as follows (figure 1(a)): ① To discretize and mesh the model, calculate the traveltime from the target zone to all receivers with the given velocity model; ② pre-processing microseismic records such as denoising and event detection, then seismograms from all receivers are mutually cross-correlated within the selected time window to generate several cross-correlograms, which contain traveltime difference information; ③ to operate elastic interferometric migration on every cross-correlogram;
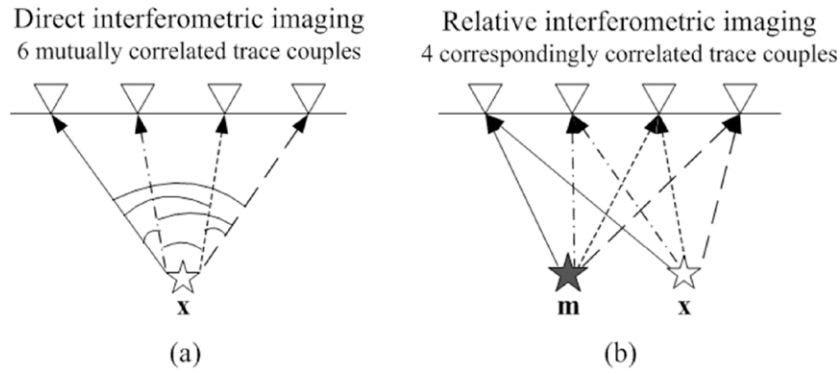
Direct interferometric imaging
6 mutually correlated trace couples   Relative interferometric imaging
4 correspondingly correlated trace couples

(a)   (b)

Figure 1. Schematic for (a) direct and (b) relative interferometric imaging (taking four receivers as the example).
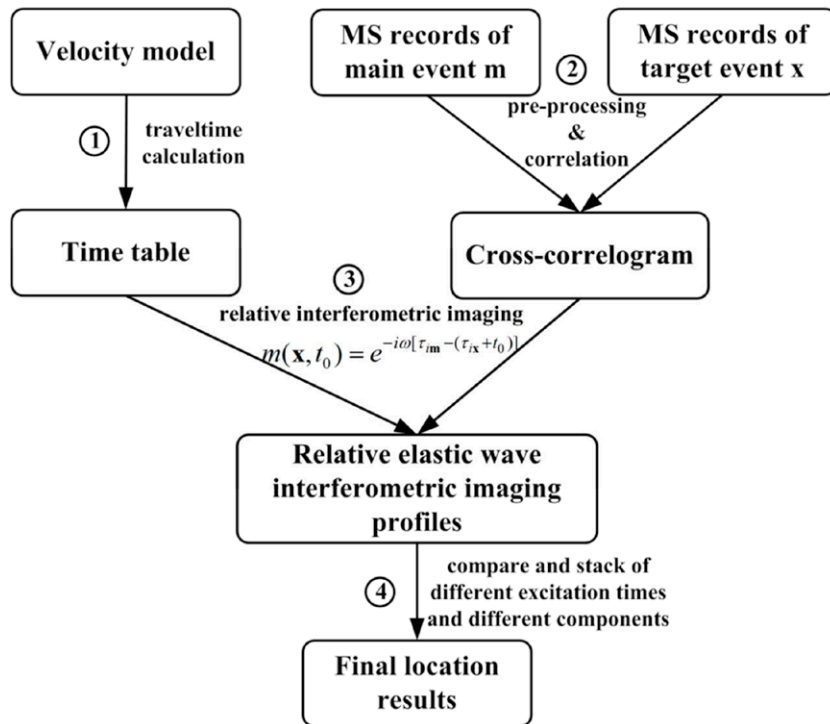
Velocity model

MS records of main event m ② **MS records of target event x**

① traveltime calculation

pre-processing & correlation

Time table

Cross-correlogram

③ relative interferometric imaging
$m(\mathbf{x}, t_0) = e^{-i\omega[\tau_{im} - (\tau_{ix} + t_0)]}$

Relative elastic wave interferometric imaging profiles

④ compare and stack of different excitation times and different components

Final location results

Figure 2. Flowchart of REII. 'MS' stands for 'microseismic'.

④ to stack all the migration profiles to obtain the final source imaging profile. The above operations are conducted with different components individually, but simultaneously. ⑤ Finally, imaging profiles of all components can be compared and stacked to ensure and validate the location results. In order to distinguish the conventional interferometric imaging from our newly proposed REII, we call it direct elastic interferometric imaging (DEII). The formula for DEII is seen as (Schuster *et al* 2004, Li *et al* 2015):

$$M_{\mathrm{D}}(\mathbf{x}) = \sum_{A,B}\sum_{\omega} \widetilde{\phi}(A, B)m(\mathbf{x}) = \sum_{A,B} \phi(A, B, \tau_{B\mathbf{x}} - \tau_{A\mathbf{x}}),$$

$$\tau_{B\mathbf{x}} - \tau_{A\mathbf{x}} = [(t_{AP} - t_{BS}), (t_{AP} - t_{BP}), (t_{AS} - t_{BS}), (t_{AS} - t_{BP})]$$

$$\Big|_{\mathbf{x}} = [\Delta t_{PS}, \Delta t_{PP}, \Delta t_{SS}, \Delta t_{SP}]\Big|_{\mathbf{x}} \qquad (1)$$

where $\widetilde{\phi}(A, B)$ and $\phi(A, B)$ are cross-correlation functions of two arbitrary traces A and B in frequency domain and time domain, respectively, $m(\mathbf{x}) = e^{-i\omega(\tau_{B\mathbf{x}} - \tau_{A\mathbf{x}})}$ is the migration kernel function, $\mathbf{x}$ is the source location vector, $\tau_{B\mathbf{x}} - \tau_{A\mathbf{x}}$ stands for the term of traveltime differences of direct waves, Δt_{PS} is the traveltime difference between P-wave and S-wave of two arbitrary traces, and Δt_{PP}, Δt_{SS} and Δt_{SP} have similar meanings. In practice, according to the characteristics of field microseismic data, a weighting coefficient can be multiplied into the term of traveltime difference to improve the location precision (Li *et al* 2015). The imaging value $M_{\mathrm{D}}(\mathbf{x})$ will reach its maximum when $\mathbf{x}$ reaches the true source location. In consideration of the probable errors of the traveltime calculation algorithm and velocity model, and to improve the stability and reliability of the method, the traveltime difference is replaced by a time window $[-w\Delta t, w\Delta t]$, where w is half the length of the time window, and it is centered at $\tau_{B\mathbf{x}} - \tau_{A\mathbf{x}}$. Equation (1) becomes the time-window-based formula of DEII:
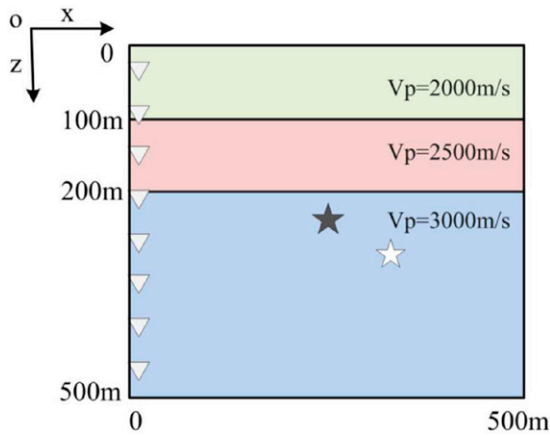
Figure 3. 2D horizontally layered velocity mode and the source-receiver geometry. Inverted triangle '∇' represents the receiver and the star '$\star$' represents the source; the black one indicates the main event and the white one indicates the target event.

$$M_{\mathrm{D}}(\mathbf{x}) = \sum_{A,B} \sum_{n=-w}^{w} \phi(A, B, \tau_{B\mathbf{x}} - \tau_{A\mathbf{x}} + n\Delta t). \qquad (2)$$

By uniting the relative location method and the above-mentioned direct interferometric imaging, we propose a new REII method, which can obtain both source location and excitation time. Its principles and procedures are as follows in (figures 1(b) and 2): ① The two steps are the same as in DEII, i.e. to discretize and mesh the model, to calculate traveltime and pre-process the data; ② then select a main event and extract its waveforms and traveltime in all receivers, seismograms of the main event and target event from all receivers are cross-correlated correspondingly within the selected time window to generate one cross-correlogram. The perforation shot or any located event can be considered as the main event. It can also be modeled when there is no existing seismogram of the main event. Since the excitation time is unknown, we can only predict an excitation time window based on the seismogram and velocity model. ③ To operate relative elastic interferometric migration on the cross-correlogram within the excitation time window to obtain imaging profiles. The above operations are still conducted with different components individually, but simultaneously, like those of DEII. ④ Finally, imaging profiles of all components and all potential excitation times are compared and stacked to obtain and verify the location results. Due to the complex source mechanisms induced by hydraulic fracturing or other engineering operations (Artman *et al* 2010, Zhebel and Eisner 2015), envelopes of cross-correlation traces are utilized to eliminate the effects of changing polarities resulting from the source mechanism (Baker *et al* 2005, Gharti *et al* 2010, Luo and Wu 2013). The time-window-based formula of REII can be obtained on the basis of equation (2):

$$M_{\mathrm{R}}(\mathbf{x}, t_0) = \sum_{i} \sum_{n=-w}^{w} \phi_{\mathrm{e}}(i, i^{\mathbf{m}}, [\tau_{i\mathbf{m}} - (\tau_{i\mathbf{x}} + t_0) + n\Delta t]) \qquad (3)$$

where ϕ_{e} is the envelope of the cross-correlogram of the main event and target event, **m** and **x** are their source location

vectors, $\tau_{i\mathbf{m}} - (\tau_{i\mathbf{x}} + t_0)$ stands for the traveltime differences term, which contains the unknown excitation time t_0, and it means the traveltime difference of the positions of the two events to the same receiver i (figure 1(b)). The meanings for other parameters are identical to those of equation (2). The imaging value $M_{\mathrm{R}}(\mathbf{x}, t_0)$ will reach its maximum when **x** is the true source location and t_0 is the true excitation time. REII inherits advantages from both the relative location method and direct interferometric imaging. It makes good use of the known information of located events, and can also flexibly choose different imaging solutions.

To sum up, traveltime differences from the position of the same potential event to different receivers are used in direct interferometric imaging (figure 1(a)), while relative interferometric imaging utilizes those of different events to the same receiver (figure 1(b)). Both methods image the source by adopting interferometric imaging on the cross-correlogram. In the next section, several numerical experiments are conducted to compare and verify the feasibility and reliability of both methods. The effects of source mechanism, receiver configuration and velocity model errors are also investigated.

3. Numerical examples

In this study, the staggered-grid finite-difference method is used to simulate microseismic records (Vireux 1986, Dong *et al* 2000), and the eikonal solver package FDTIMES is used to calculate the traveltime of the first arrivals (Podvin and Lecomte 1991).

3.1. 2D model

Under 2D conditions, a horizontally layered isotropic model (figure 3) and a single-point force are used to simulate elastic microseismic wavefields and records. The size of the model is 500×500 m, and the depths of the two interfaces are 100 and 200 m, respectively. The space and time spacing are 2.5 m and 0.5 ms, respectively. The velocities of P-wave and the density of three layers from the top to bottom are (2000 m s^{-1}, 2 g cm^{-3}), (2500 m s^{-1}, 2.5 g cm^{-3}), (3000 m s^{-1}, 3 g cm^{-3}), respectively, and the $V_{\mathrm{P}}/V_{\mathrm{S}}$ ratio is 1.67. The source is a Ricker wavelet function with a center frequency of 60 Hz. For downhole monitoring with a single vertical well, 51 receivers with 10 m spacing are placed along the depth direction.

To testify to the feasibility of relative interferometric imaging in a microseismic location, a vertical single-point force source is modeled and located. The main event and target event are set at (250 m, 250 m) and (350 m, 325 m), respectively. The main event is also a vertical single-point force, and the excitation time of the target event is 15 ms. The predicted excitation time window is (1 ms, 80 ms) and the step size is 1 ms. The seismogram of the V_x component is shown in figure 4, and obvious events and multiples can be seen on it. The amplitudes and polarities are changing due to both the source mechanism and source–receiver geometry.
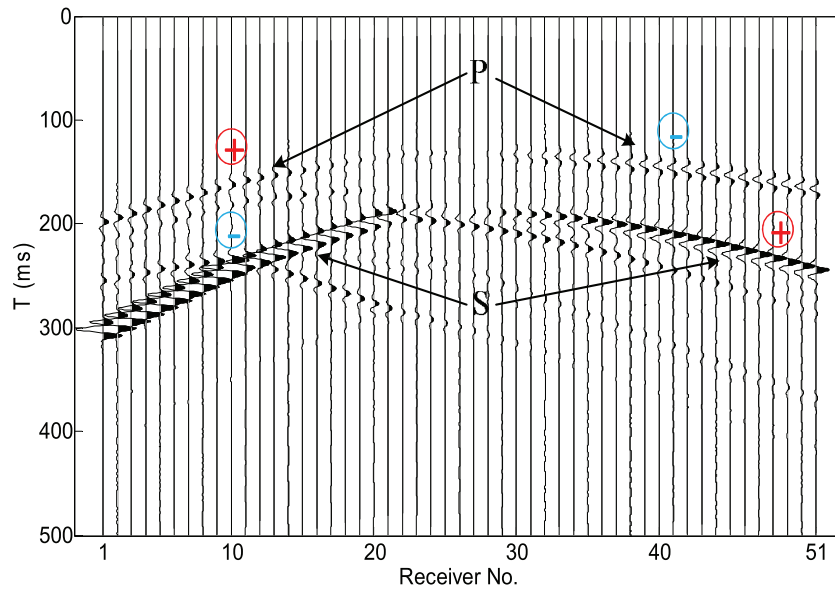
Figure 4. The simulated seismogram of the V_x component from downhole monitoring. The circled '+' and '−' represent positive polarity and negative polarity, respectively.
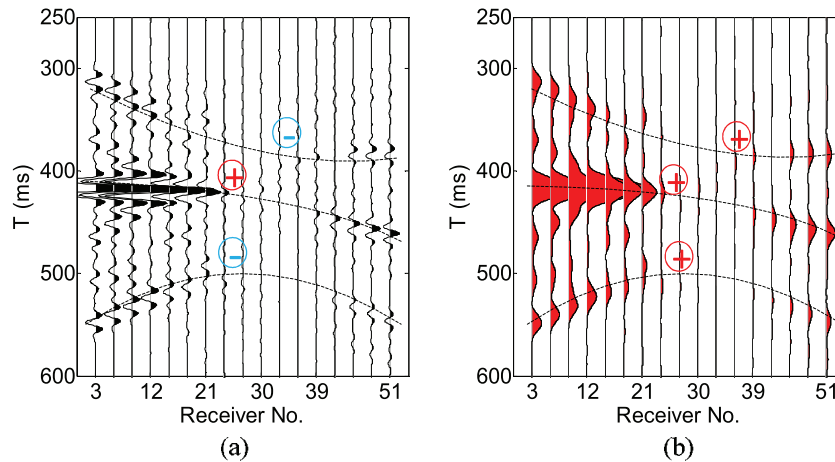

Figure 5. (a) Partial cross-correlation traces of the V_x component before being enveloped. (b) Partial cross-correlation traces of the V_x component after being enveloped. Note that only three events are clearly seen, and the P-wave and P-wave cross-correlation term is hidden, as a consequence of its weak amplitudes and closeness with the S-wave and S-wave cross-correlation term.

Figure 5(a) presents partial cross-correlation traces of the V_x component. The changing polarities in the original seismograms lead to changing polarities in the cross-correlation traces. The three dashed curves represent the terms of S-wave and P-wave cross-correlation, S-wave and S-wave cross-correlation and P-wave and S-wave cross-correlation, respectively. The P-wave and P-wave cross-correlation term is quite weak and we propose to eliminate the small correlation values by multiplying a weighting coefficient $W = [1, 0, 1, 1]$ into the traveltime difference term to improve the location precision (Li *et al* 2015).

Relative interferometric imaging results of a vertical single-point force are shown in figure 6. Here, figures 6(a)–(c) are the results of the V_x, V_z and stacking components by REII with the original cross-correlogram. The stacking component is generated by multiplying the imaging results of the V_x and V_z components (multiplying can highlight the common large imaging value of different components). Although the imaging profiles have high resolution, the accuracy and reliability are affected by changing polarities of the cross-correlation waveforms (figure 6(a)). Both positive and negative values arise around the locations.

We adopt the envelopes of the cross-correlation waveforms to overcome the effect of changing polarities (equation (3)). Figure 5(b) presents partial cross-correlation traces of the V_x component after being enveloped. All of the amplitudes turn into positive values. Figures 6(d)–(f) are the results of the V_x, V_z and stacking components by REII with the enveloped cross-correlogram. On the one hand, the imaging resolution of the enveloped cross-correlogram becomes lower, since enveloping reduces the frequency of waveforms. On the other hand, enveloping overcomes the effects of changing polarities and makes the imaging more stable and reliable. Figure 7 shows the detailed process to obtain the relative interferometric imaging result in figure 6(f). We compared the maximum imaging values of all predicted excitation times (figures 7(a)
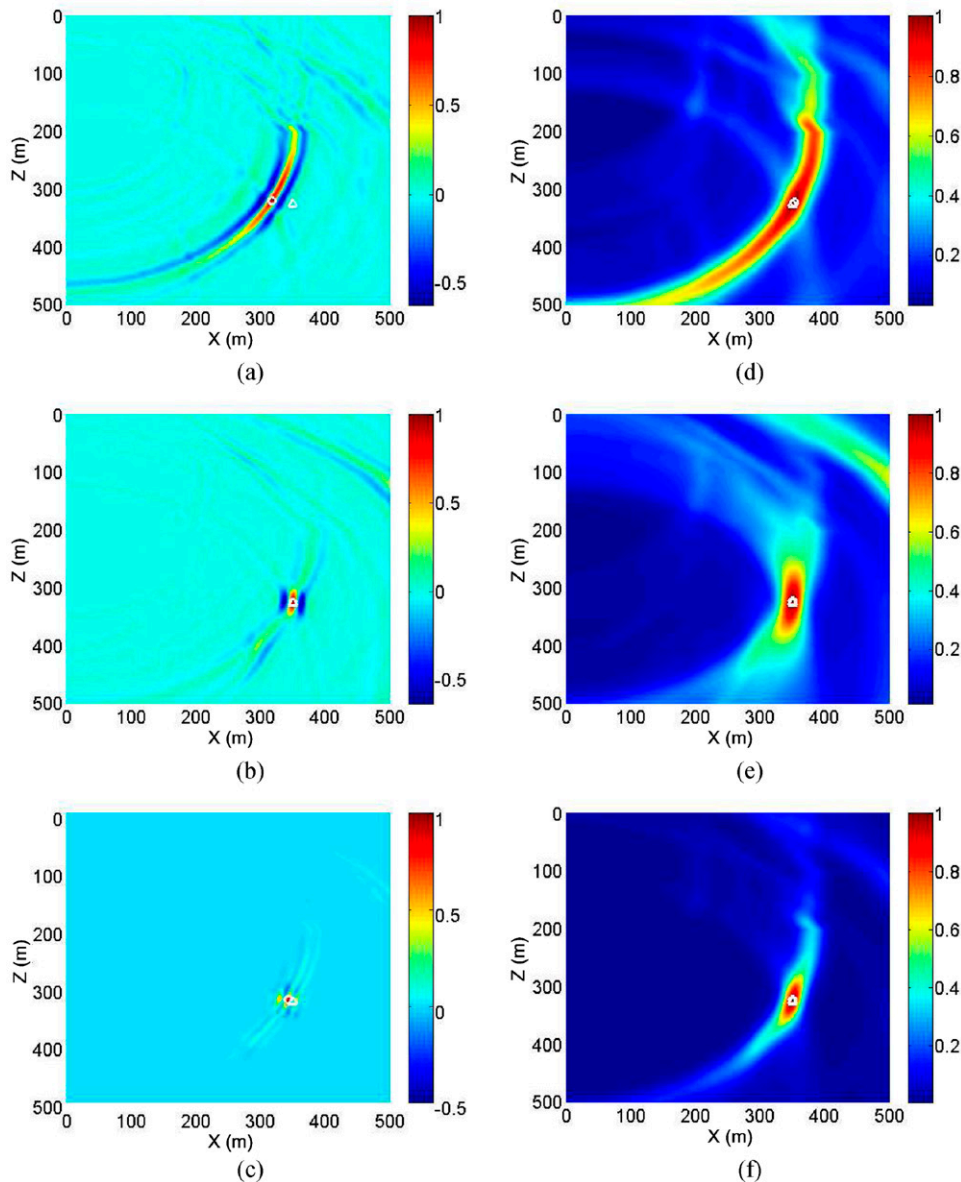
Figure 6. Relative interferometric imaging results of a vertical single-point force. (a)–(c) Results of the V_x, V_z and stacking components by REII with the original cross-correlogram. (d)–(f) Results of the V_x, V_z and stacking components by REII with the enveloped cross-correlogram. The white triangle 'Δ' indicates the true source position; the white circle '$\bigcirc$' indicates the imaging location.

and (b)) and chose the profile with maximum value as the final location profile.

The above 2D numerical examples demonstrate the feasibility of REII. The validity of the envelope of cross-correlation traces in overcoming the effects of changing polarities proposed in this study has also been proved.

3.2. 3D model

For the 3D case, the numerical source implementation can be learned from seismology. Representations of earthquake sources can be included in the staggered-grid finite difference method using either the velocity components (Graves 1996) or the stress components (Pitarka 1999). In this study, a moment tensor source formulation of double-couple source is simulated with a distribution of body forces that are added to stress components. Although double-couple source exhibits distinct

polarity changes (Rutledge and Phillips 2003, Chapman and Leaney 2012, Zhebel and Eisner 2015), there are many non-double-couple components in source mechanisms induced in hydraulic fracturing (Ross *et al* 1996, Šílený *et al* 2009).

A horizontally layered isotropic model is still used. The size of the model is $200 \times 200 \times 200$ m, and depths of the two interfaces are 50 and 150 m, respectively. The time spacing is 0.3 ms and the other model parameters are the same as those of the 2D model. The main event is set at (100 m, 100 m, 100 m), while the target event is set at (125 m, 75 m, 100 m), and we assume that the excitation time is known. For simplicity, a dip-slip source mechanism with a strike of 0°, dip of 90°, and rake of 90° is modeled, which is simulated with a Ricker wavelet of 60 Hz. To investigate the effect of the receiver configuration on REII, single-well, double-well and surface monitoring are simulated and imaged. The receiver spacing is still 10 m. For single-well monitoring, 21 receivers are placed along
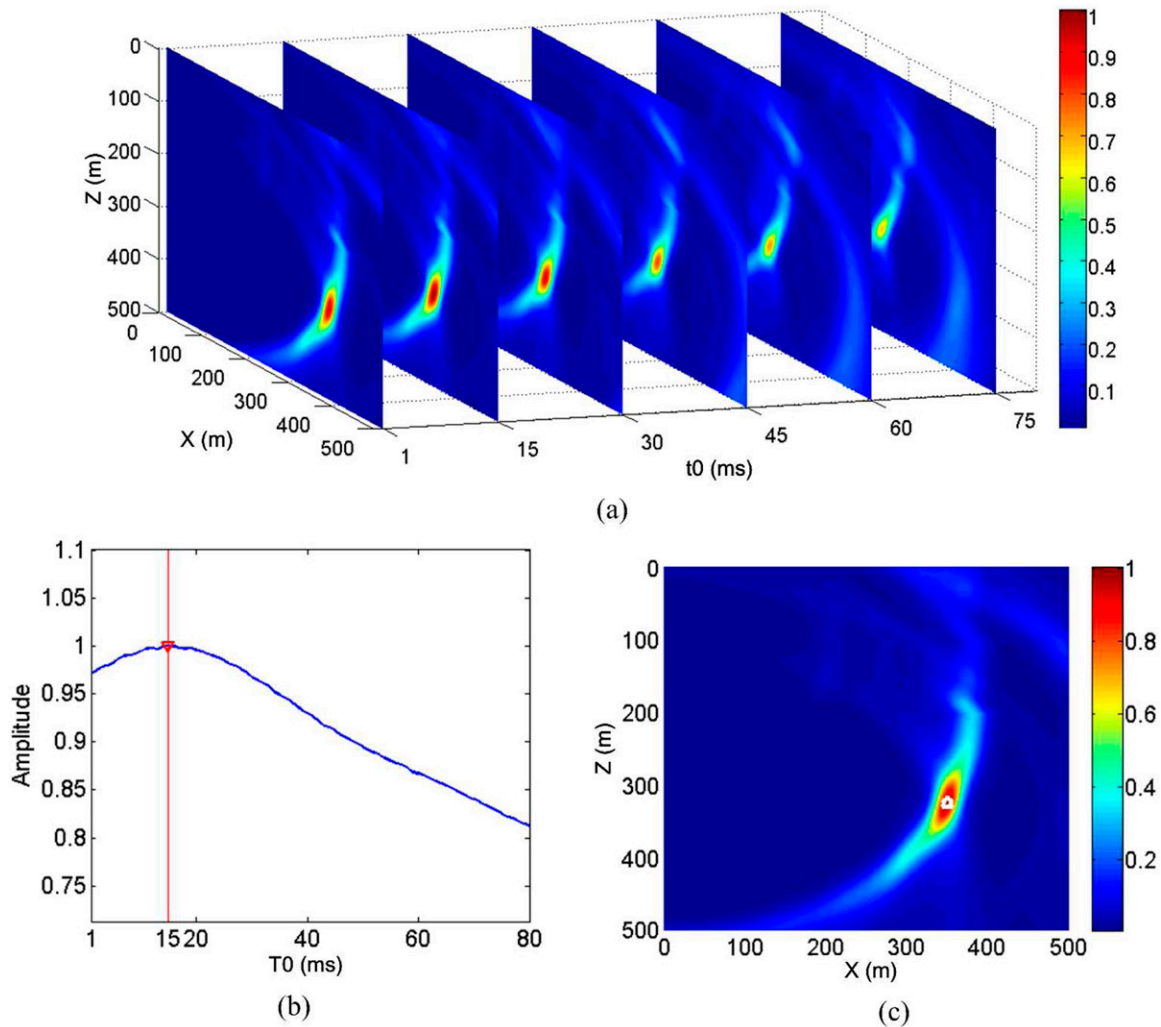
Figure 7. Relative interferometric imaging result of the stacking component of a vertical single-point force. (a) 3D slice view of imaging profiles of the stacking component that correspond to the partial predicted excitation times. (b) The curve of different excitation times and their corresponding maximum imaging values. (c) The final location profile.

the depth direction at $X = 0$ m and $Y = 0$ m. For double-well monitoring, another vertical array at $X = 0$ m and $Y = 200$ m is added. For surface monitoring, two orthogonal arrays with 21 receivers are placed at $X = 100$ m and $Y = 100$ m, respectively. Although star-array or rectangle-array is usually utilized in field surface monitoring, the simplified orthogonal arrays adopted here can also be used to verify the feasibility of the method. Figure 8 shows the 3D horizontally layered velocity model and the source–receiver geometry.
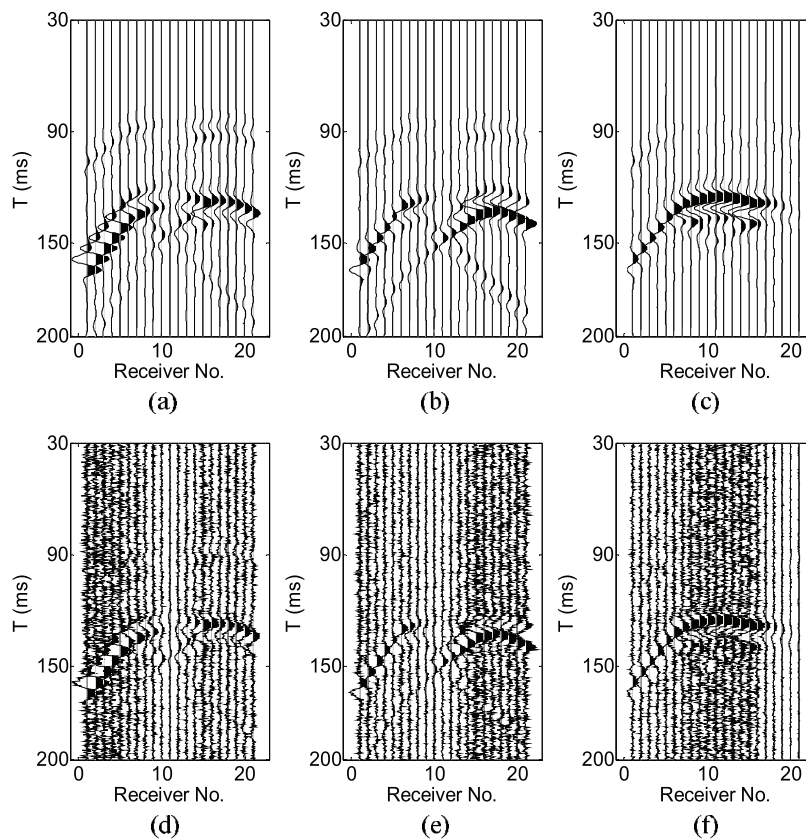
Figures 9(a)–(c) are synthetic three-component seismograms of the downhole array. Given that field microseismic data contain massive noise, random noise has been added into the synthetic data. Figures 9(d)–(f) are seismograms with random noise. The SNR reduces to 0.1 dB after adding the noises (SNR $= 10 * \log_{10}(\overline{S}/\overline{N})$, $\overline{S}$ and $\overline{N}$ are the average energy for signal and noise, respectively). The imaging result of the stacking component by REII with an enveloped cross-correlogram for the single-well monitoring is shown in figure 10.

Note that there exist obvious arc narrow band artifacts in the X–Y profile. They result from the limited horizontal
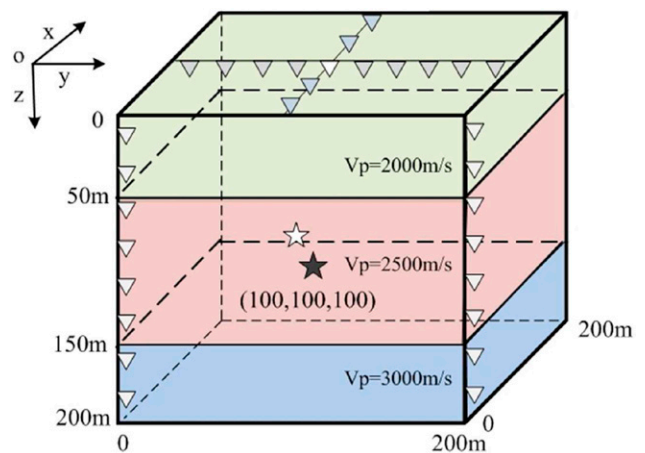

Figure 8. 3D horizontally layered velocity model and the source–receiver geometry.

coverage of single-well monitoring, which results in limited azimuth resolution. The more detailed reason is that the traveltimes around the monitoring well in the X–Y plane to the same receiver are identical. The azimuth can be estimated by

Figure 9. Synthetic three-component seismograms of the downhole array. (a)–(c) Noise-free seismograms of the V_x, V_y and V_z components, respectively. (d)–(f) Seismograms with random noise (SNR = 0.1 dB).
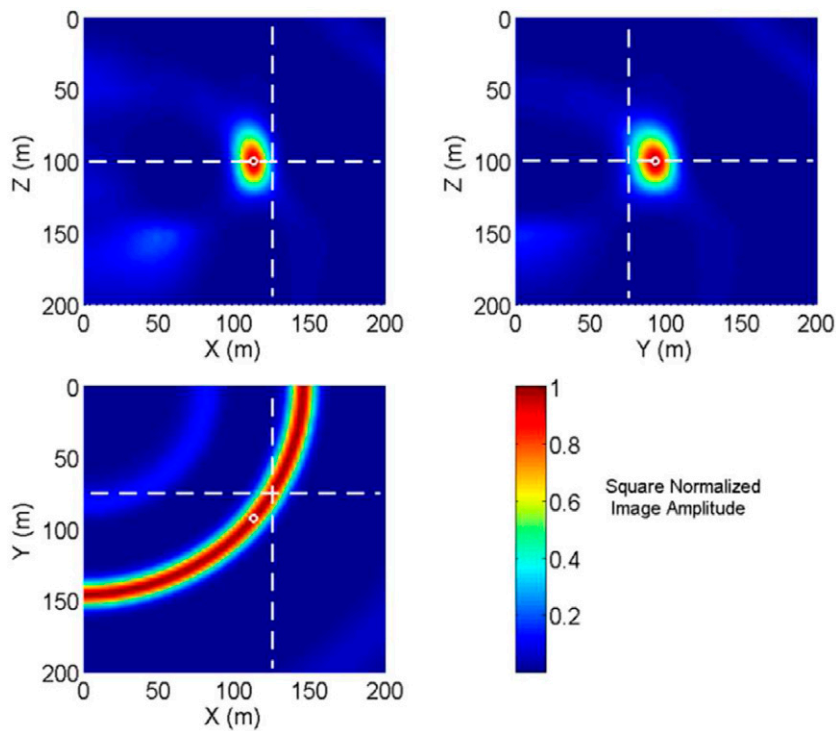
Figure 10. Imaging result of the stacking component by REII with an enveloped cross-correlogram. The cross points of white dashed lines indicate the true source positions; the white circles '○' indicate the imaging locations.
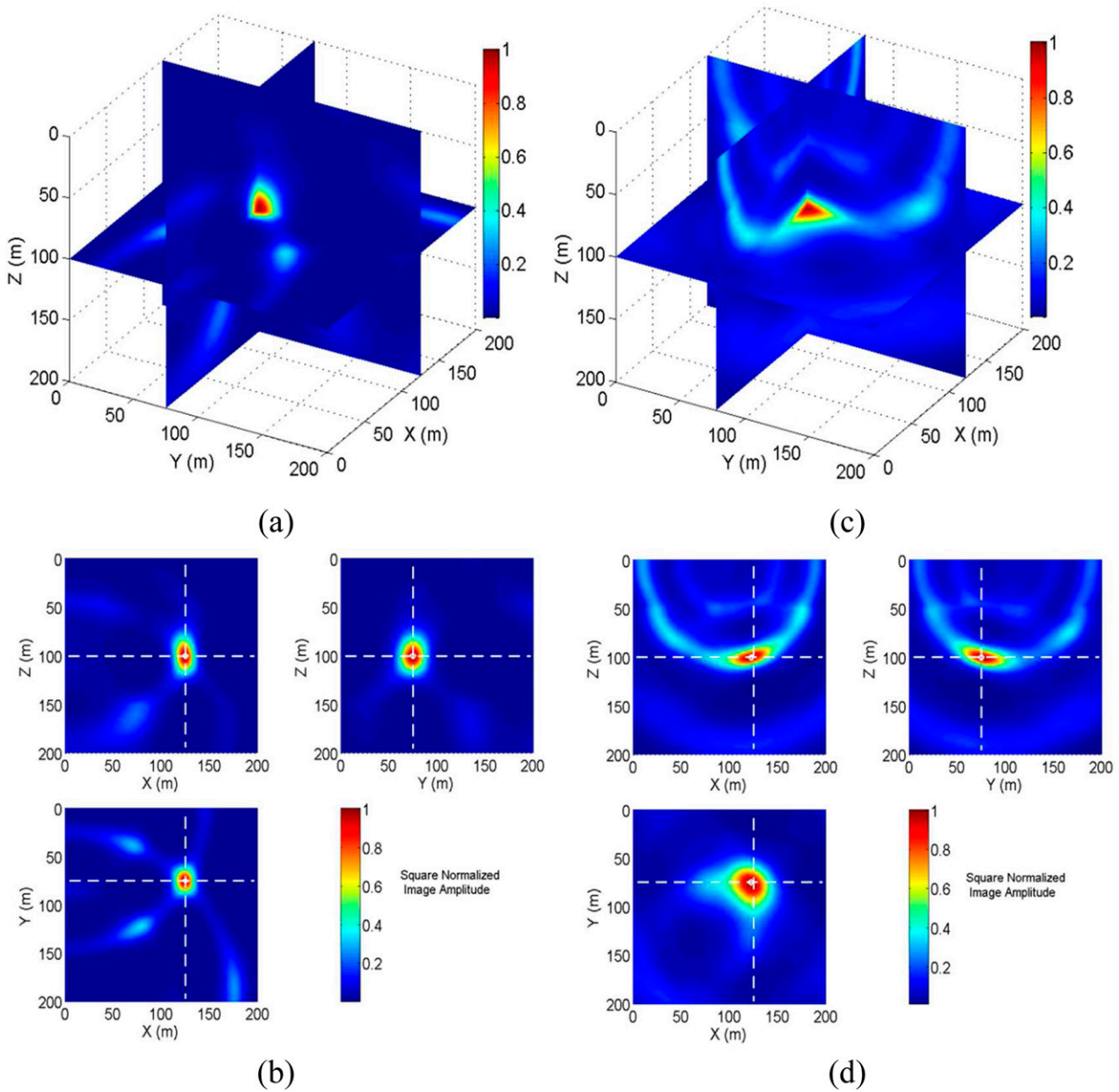
Figure 11. 3D ((a) and (c)) and 2D ((b) and (d)) view of the imaging results for double-well and surface monitoring. The left column ((a) and (b)) is the result of double-well monitoring, while the right column ((c) and (d)) is the result of surface monitoring. The results of the two monitoring arrays both have good imaging resolution, as well as some imaging disturbances, which result from acquisition footprint.

analyzing the polarization of the three-component records or improving the extent of image focusing with more azimuthal constraints.

Next, seismograms with added noise from double-well (SNR = 0.1 dB) and surface arrays (SNR = −15 dB) are used by REII with an enveloped cross-correlogram to image the source. The results are shown in figures 11(a)–(d). For both double-well and surface arrays, the artifacts in the *X–Y* profile are attenuated or eliminated. When the number of monitoring wells, and receivers or the apertures of the monitoring arrays are increased, the constraint conditions in the imaging process are consequently increased. The result becomes more convergent, and thus the artifacts are suppressed and location precision is improved. However, the computational expenses

(including calculation time and requisite memory space) are also increased.

Finally, the effects of velocity model errors (traveltime errors) on location results and computational expenses of REII and DEII have been tested. It should be noted that except for the velocity model, the main event location and monitoring array configuration can also affect location results. For simplicity, ±5%, ±10% and ±15% errors are directly added into the theoretical traveltime, instead of the velocity model. The target event is set at (125 m, 75 m, 70 m), double-well monitoring is adopted, and the other parameters are as in the above numerical experiment. The location results and computational expenses are shown in figures 12 and 13 and table 1.
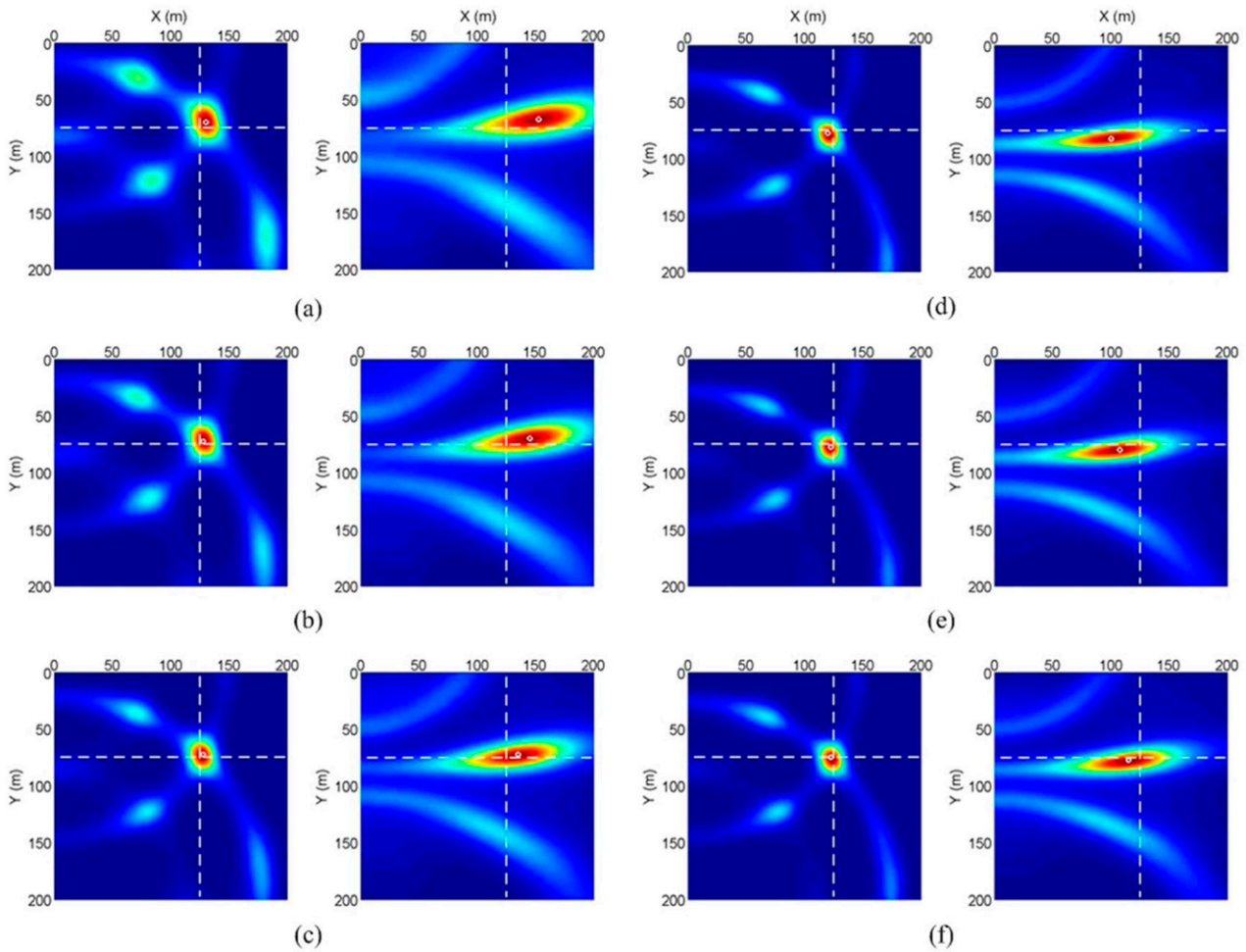
Figure 12. Comparison of location results (*X–Y* profile). Left of (a)–(f): *X–Y* imaging profile for REII of −15%, −10%, −5%, 15%, 10%, 5% theoretical traveltime error, respectively. Right of (a)–(f): *X–Y* imaging profile for DEII of −15%, −10%, −5%, 15%, 10%, 5% theoretical traveltime error, respectively.
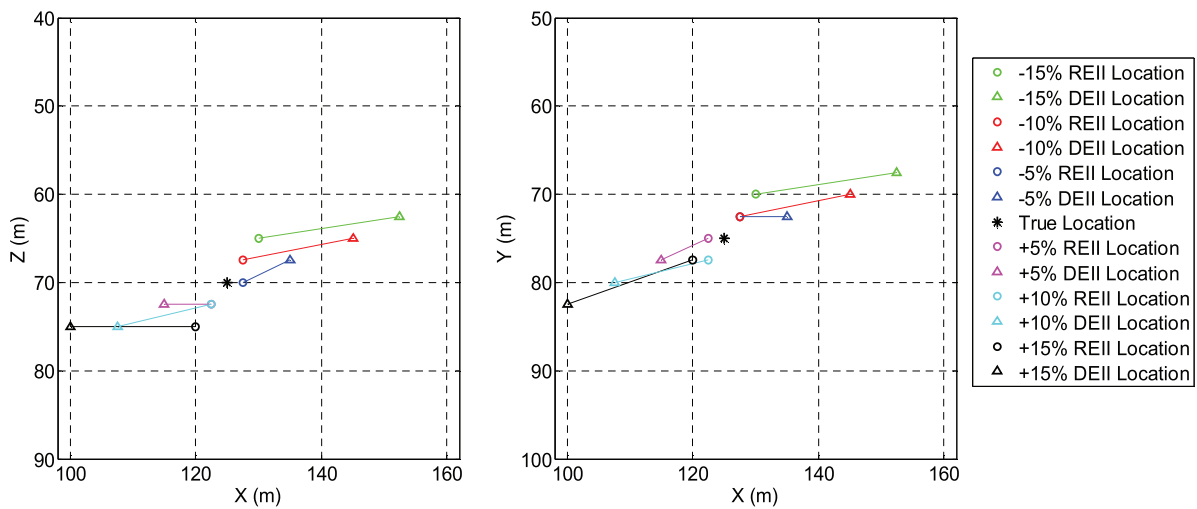
Figure 13. Plan-view of location results.

It is obvious that REII has much higher imaging resolution and fewer location errors compared with DEII. Since the given main and target events have similar or coincident traveling paths, the uncertainty of velocity is largely alleviated through the subtraction of traveltimes (cross-correlation of waveforms), so REII is less sensitive to the traveltime/velocity errors (Poliannikov *et al* 2013). Moreover, the computational time has been greatly decreased, since far fewer cross-correlogram traces have been generated and imaged. Thus, the requisite memory space is also smaller for REII.

Table 1. Comparison of location results and computational expenses.

Theoretical traveltime error	Location error (m)	
	REII	DEII
−15%	8.66	29.47
−10%	4.33	21.21
−5%	3.54	10.61
0	0	0
+5%	3.54	10.61
+10%	4.33	18.87
+15%	5.59	26.58
Calculation time	~180 s	~8440 s
Memory space	~6.3 GB	~8.2 GB

Note: A computer with an Intel i7-4790 3.6 GHz, and RAM 32GB, is used for the calculation.

4. Conclusion

An REII method for microseismic source location is proposed through combining the relative location method and DEII. The traveltime differences between the known main event and all potential sources with respect to the receiver array are calculated. Then, the cross-correlogram of the main event and target event is interferometrically imaged. Numerical experiments on 2D and 3D models demonstrate the feasibility of this newly proposed method. Envelopes of cross-correlation traces are adopted to overcome the effects of changing polarities resulting from the source mechanism and receiver configuration. Compared with direct interferometric imaging in the 3D numerical experiment of double-well monitoring, relative interferometric imaging exhibits higher calculation efficiency and reliability with a certain amount of theoretical traveltime error.

Acknowledgments

References

Artman B, Podladtchikov I and Witten B 2010 Source location using time-reverse imaging *Geophys. Prospect.* **58** 861–73

Baker T, Granat R and Clayton R W 2005 Real-time earthquake location using Kirchhoff reconstruction *Bull. Seism. Soc. Am.* **95** 699–707

Bardainne T, Gaucher E, Cerda F and Drapeau D 2009 Comparison of picking-based and waveform-based location methods of microseismic events: application to a fracturing job *79th SEG Annual Meeting* pp 1547–51 (Expanded Abstracts)

Borcea L, Papanicolaou G and Tsogka C 2006 Coherent interferometric imaging in clutter *Geophysics* **71** SI165–75

Campillo M and Paul A 2003 Long-range correlations in the diffuse seismic coda *Science* **299** 547–9

Chambers K, Dando B D E, Jones G A, Velasco R and Wilson S A 2014 Moment tensor migration imaging *Geophys. Prospect.* **62** 879–96

Chang X, Liu Y K, Wang H and He R Q 2009 Seismic interferometric migration and data-referenced-only migration *Chin. J. Geophys.-Chin. Ed.* **52** 2840–5

Chapman C and Leaney W 2012 A new moment-tensor decomposition for seismic events in anisotropic media *Geophys. J. Int.* **188** 343–70

Cipolla C L, Maxwell S C, Mack M and Downie R 2012 A practical guide to interpreting microseismic measurements *SPE/EAGE European Unconventional Resources Conf. and Exhibition* (SPE) p 144067

Cipolla C L, Williams M J, Weng X, Mack M and Maxwell S C 2010 Hydraulic fracture monitoring to reservoir simulation: maximizing value *2nd Middle East Tight Gas Reservoirs Workshop* (SPE) p 133877

Claerbout J F 1968 Synthesis of a layered medium from its acoustic transmission response *Geophysics* **33** 264–9

Dong L G, Ma Z T, Cao J Z, Wang H Z, Geng J H, Lei B and Xu S Y 2000 A staggered-grid high-order difference method of one-order elastic wave equation *Chin. J. Geophys-Chin. Ed.* **43** 411–9

Duncan P M and Eisner L 2010 Reservoir characterization using surface microseismic monitoring *Geophysics* **75** 75A139–46

Feng G L, Feng X T, Chen B R, Xiao Y X and Jiang Q 2015 Sectional velocity model for microseismic source location in tunnels *Tunn. Undergr. Space Technol.* **45** 73–83

Fitch T J 1975 Compressional velocity in source regions of deep earthquakes: an application of the master earthquake technique *Earth Planet. Sci. Lett.* **26** 156–66

Gharti H N, Oye V, Roth M and Kühn D 2010 Automated microearthquake location using envelope stacking and robust global optimization *Geophysics* **75** MA27–46

Gibowicz S J and Kijko A 1994 *An Introduction to Mining Seismology* (San Diego, CA: Academic)

Grandi S and Oates S J 2009 Microseismic event location by cross-correlation migration of surface array data for permanent reservoir monitoring *71st EAGE Conf. and Exhibition* p X012 (Extended Abstracts)

Graves R W 1996 Simulating seismic wave propagation in 3D elastic media using staggered-grid finite differences *Bull. Seism. Soc. Am.* **86** 1091–106

Grechka V and Zhao Y 2012 Microseismic interferometry *TLE* **31** 1478–83

Grechka V, Singh P and Das I 2011 Estimation of effective anisotropy simultaneously with locations of microseismic events *Geophysics* **76** WC143–55

Grigoli F, Cesca S, Amoroso O, Emolo A, Zollo A and Dahm T 2014 Automated seismic event location by waveform coherence analysis *Geophys. J. Int.* **196** 1742–53

Grigoli F, Cesca S, Vassallo M and Dahm T 2013 Automated seismic event location by travel-time stacking: an application to mining induced seismicity *Seismol. Res. Lett.* **84** 666–77

Kao H and Shan S J 2004 The source-scanning algorithm: mapping the distribution of seismic sources in time and space *Geophys. J. Int.* **157** 589–94

Kao H and Shan S J 2007 Rapid identification of earthquake rupture plane using source-scanning algorithm *Geophys. J. Int.* **168** 1011–20

Le Calvez J H, Craven M E, Klem R C, Baihly J D, Bennett L A and Brook K 2007 Real-time microseismic monitoring of hydraulic fracture treatment: a tool to improve completion and reservoir management *SPE Hydraulic Fracturing Technology Conf.* (SPE) p 106159

Li J, Zhang H, Rodi W L and Toksoz M N 2013 Joint microseismic location and anisotropic tomography using differential arrival times and differential backazimuths *Geophys. J. Int.* **195** 1917–31

Li L, Chen H and Wang X M 2015 Weighted-elastic-wave interferometric imaging of microseismic source location *Appl. Geophys.* **12** 221–34

Luo J and Wu R S 2013 Envelope inversion—some application issues *83rd SEG Annual Meeting* pp 1042–7

Maxwell S C 2014 *Microseismic Imaging of Hydraulic Fracturing* (Tulsa: Society of Exploration Geophysicists) (doi:10.1190/1.9781560803164)

Maxwell S C, Rutledge J, Jones R and Fehler M 2010 Petroleum reservoir characterization using downhole microseismic monitoring *Geophysics* **75** 75A129–37

Pitarka A 1999 3D elastic finite-difference modeling of seismic motion using staggered grids with nonuniform spacing *Bull. Seism. Soc. Am.* **89** 54–68

Podvin P and Lecomte I 1991 Finite difference computation of traveltimes in very contrasted velocity models: a massively parallel approach and its associated tools *Geophys. J. Int.* **105** 271–84

Poliannikov O V, Malcolm A E, Djikpesse H and Prange M 2011 Interferometric hydrofracture microseism localization using neighboring fracture *Geophysics* **76** WC27–36

Poliannikov O V, Prange M, Malcolm A and Djikpesse H 2013 A unified Bayesian framework for relative microseismic location *Geophys. J. Int.* 557–71

Ross A, Foulger G and Julian B R 1996 Non-double-couple earthquake mechanisms at the geysers geothermal area, California *Geophys. Res. Lett.* **23** 877–80

Rutledge J T and Phillips W S 2003 Hydraulic stimulation of natural fractures as revealed by induced microearthquakes, Carthage Cotton Valley gas field, east Texas *Geophysics* **68** 441–52

Schuster G T 2001 Theory of daylight/interferometric imaging: tutorial *63rd EAGE Conf. and Exhibition* p A32 (Expanded Abstracts)

Schuster G T and Zhou M 2006 A theoretical overview of model-based and correlation-based redatuming methods *Geophysics* **71** SI103–10

Schuster G T, Yu J and Sheng J 2004 Interferometric/daylight seismic imaging *Geophys. J. Int.* **157** 838–52

Šílený J, Hill D P, Eisner L and Cornet F H 2009 Non-double-couple mechanisms of microearthquakes induced by hydraulic fracturing *J. Geophys. Res.* **114** B08307

Song F, Warpinski N R and Toksöz M N 2014 Full-waveform based microseismic source mechanism studies in the Barnett Shale: linking microseismicity to reservoir geomechanics *Geophysics* **79** KS13–30

Spence W 1980 Relative epicenter determination using P-wave arrival-time differences *Bull. Seism. Soc. Am.* **70** 171–83

Staněk F, Anikiev D, Valenta J and Eisner L 2015 Semblance for microseismic event detection *Geophys. J. Int.* **201** 1362–9

Tian Y and Ritzwoller M H 2015 Directionality of ambient noise on the Juan de Fuca plate: implications for source locations of the primary and secondary microseisms *Geophys. J. Int.* **201** 429–43

Vireux J 1986 P-SV wave propagation in heterogeneous media: velocity stress finite-difference method *Geophysics* **51** 889–901

Waldhauser F and Ellsworth W L 2000 A double-difference earthquake location algorithm: method and application to the northern Hayward fault, California *Bull. Seism. Soc. Am.* **90** 1353–68

Wapenaar K, Draganov D and Snieder R 2010a Tutorial on seismic interferometry: part 1—basic principles and applications *Geophysics* **75** 75A195–209

Wapenaar K, Slob E and Snieder R 2010b Tutorial on seismic interferometry: part 2—underlying theory and new advances *Geophysics* **75** 75A211–27

Warpinski N 2014 Microseismic monitoring—the key is integration *TLE* **33** 1098–106

Xiao X, Luo Y, Fu Q, Jervis M, Dasgupta S and Kelamis P 2009 Locate microseismicity by seismic interferometry *EAGE Passive Seismic Workshop-Exploration and Monitoring Applications* p A22

Zhang H J and Thurber C H 2003 Double-difference tomography: the method and its application to the Hayward fault, California *Bull. Seism. Soc. Am.* **93** 1875–89

Zhang W and Zhang J 2013 Microseismic migration by semblance-weighted stacking and interferometry *83rd SEG Annual Meeting* pp 2045–9

Zhao X and Young R P 2011 Numerical modeling of seismicity induced by fluid injection in naturally fractured reservoirs *Geophysics* **76** WC167–80

Zhebel O and Eisner L 2015 Simultaneous microseismic event localization and source mechanism determination *Geophysics* **80** KS1–9